Research Article

Water hyacinth derived carbon quantum dots and g-C_3N_4 composites for sunlight driven photodegradation of 2,4-dichlorophenol

Chen Hong Hak[1] · Kah Hon Leong[1] · Yik Heng Chin[1] · Pichiah Saravanan[2] · Sin Tee Tan[3] · Woon Chan Chong[4] · Lan Ching Sim[4]

Received: 23 January 2020 / Accepted: 28 April 2020 / Published online: 7 May 2020

Abstract
Carbon dots (CDs) were successfully derived from water hyacinth leaves and the binary composite was achieved by incorporating CDs with g-C_3N_4 through hydrothermal treatment. The average particle size of CDs was found to be 3.1 nm and a blue-green fluorescence was emitted under the UV light irradiation. Both of the composites loaded with 20 wt.% (20CDs/g-C_3N_4) and 40 wt.% (40CDs/g-C_3N_4) of CDs achieved the highest degradation efficiency of 2,4-dichlorophenol (2,4-DCP) with 1.7 times higher than that of pure g-C_3N_4. This work successfully improved the properties of g-C_3N_4 by elongating the lifetime of photogenerated electrons and widening the visible light response. Both of 20CDs/g-C_3N_4 and 40CDs/g-C_3N_4 recorded the highest photocatalytic performance in degrading 2,4-DCP with degradation rate constant of 0.0194, and 0.0186 min^{-1}, respectively. This is contributed by the prolonged charge carrier lifetime in 20CDs/g-C_3N_4; good visible light absorption and high specific surface area in 40CDs/g-C_3N_4. For the scavenger test, hole (h^+) and superoxide radical ($^{\cdot}O_2^-$) were acknowledged as the key active species in photocatalysis.

Keywords Carbon quantum dots · CDs/g-C_3N_4 composite · 2,4-Dichlorophenol · Water hyacinth

1 Introduction

Conventional wastewater treatments such as coagulation, flocculation, filtration and disinfectant are not purposely designed for endocrine disrupting chemicals (EDCs) removal. In recent years, advanced oxidation processes (AOPs) have gained more concern due to its high effectiveness in degrading a large range of pollutants via the redox reactions. The fast reaction rate, mild end products and non-selective degradation with reasonable operating cost have made it become a promising technology for EDCs degradation.

Carbon dots (CDs) are tiny carbon nanoparticles with size smaller than 10 nm and were initially isolated during the purification of single-walled carbon nanotubes (SWNTs) in 2004 [1]. The properties of CDs rely on the starting material and the synthesis method. There are some unique properties of CDs, such as good electrical conductivity, strong fluorescent lifetime, electrochemiluminescence, optical stability, low toxicity and exceptional

Electronic supplementary material The online version of this article (https://doi.org/10.1007/s42452-020-2840-y) contains supplementary material, which is available to authorized users.

✉ Lan Ching Sim, simcl@utar.edu.my; Chen Hong Hak, ch.hak117@gmail.com; Kah Hon Leong, khleong@utar.edu.my; Yik Heng Chin, yhchin@utar.edu.my; Pichiah Saravanan, pichiahsaravanan@gmail.com; Sin Tee Tan, tansintee@upm.edu.my; Woon Chan Chong, chongwchan@utar.edu.my | [1]Department of Environmental Engineering, Faculty of Engineering and Green Technology, Universiti Tunku Abdul Rahman, Kampar, Perak, Malaysia. [2]Department of Environmental Science and Engineering, Indian Institute of Technology (ISM), Dhanbad, Dhanbad, Jharkhand 826004, India. [3]Department of Physics, Faculty of Science, University Putra Malaysia (UPM), 43400 Serdang, Selangor Darul Ehsan, Malaysia. [4]Department of Chemical Engineering, Lee Kong Chian Faculty of Engineering and Science, Universiti Tunku Abdul Rahman, Jalan Sungai Long 9, Bandar Sungai Long, 43000 Kajang, Selangor, Malaysia.

multi-photon excitation (up-conversion) [2–6]. The fluorescent and low toxicity of CDs enable it applicable in biosensing [7, 8], bioimaging [9, 10] and chemical sensing [11]. The carboxyl, hydroxyl and nitrogen groups attached on the surface of CDs improve the biocompatibility and optical property along with enhances the selectivity and sensitivity for metal ions [12, 13]. Furthermore, CDs have unique property which make it applicable in photocatalysis such as photo-induced electron transfer and different emissive traps on the surface of CDs arising from quantum effect [14]. These distinctive properties of CDs had motivated numerous researchers to utilize CDs in photocatalysis.

The high solubility property of CDs limits its application in the degradation of organic pollutants in aqueous solution. This limitation can be overcome by combining CDs with other semiconductor photocatalyst like TiO_2, ZnO, Fe_2O_3 and etc. Further the semiconductor can act as a supported media to attach with CDs, so that can reclaim the photocatalyst with CDs. Ke et al. [15] has studied the performance of N-doped CDs/TiO_2 in methylene blue (MB) degradation. It was reported that the degradation efficiency was 90% within 120 min, which was 3.6 times higher than the pristine TiO_2. Moreover, Yu and Kwak [16] also conducted research regarding the photocatalytic degradation of MB by using the CDs incorporated mesoporous hematite composites (CDs/MH). The photodegradation efficiency of MB was found to be 97% within 90 min. The surface area increased up to 187 m^2/g and the recombination rate of charge carriers reduced. Besides, the photocatalytic activity of CDs/Fe_2O_3 composites against benzene gas was reported by Zhang et al. [17]. The degradation efficiency of benzene gas improved from 37% (pure Fe_2O_3) to 80% (CDs/Fe_2O_3/) due to the excellent UCPL of the CDs which promoted formation of photogenerated electron–holes pairs. Besides, it was reported that the conjugate network structure enhanced the adsorption properties due to the π–π interaction between the CDs and benzene molecules. Cheng and co-workers modified aqua mesophase pitch-derived CDs with ammonia and thionyl chloride, respectively. The nitrogen doped CDs degraded 97% of RhB in 4 h with rate constant of 0.02463 min^{-1}. The photodegradation performance maintained at 93% after being reused 5 times [18].

Semiconductor graphitic carbon nitride (g-C_3N_4) is one of the most fascinating photocatalysts for the degradation of pollutants. It is well known for its moderate band gap, which is around 2.7 eV which allows absorption of light within the visible light range [19]. Owing to the narrow band gap of g-C_3N_4, the electrons can easily fall back into its original position. In this context, the fast recombination of electron–hole pair in g-C_3N_4 can be suppressed by combining g-C_3N_4 with CDs. When g-C_3N_4 and CDs are formed heterojunction, the differences in the CB and VB level between two photocatalysts causes band bending at the interface of junction. The band bending drives the photogenerated electrons and holes to move in opposite directions [20]. One of the photocatalyst will serve as an electron/hole acceptor and hence the electron will not fall back easily to VB and recombine with the holes. The coupling mechanism enables the photocatalytic application of CDs in aqueous solution by supporting the highly soluble CDs with insoluble g-C_3N_4. Furthermore, the incorporate of CDs into g-C_3N_4 could enhance the light absorption capacity in entire visible and NIR range and promote more electron-hole pairs generate.

It is always exciting to discover the green starting materials for CDs because these are easily accessible, inexpensive, non-toxic and clean. Recently, some achievements have been accomplished by utilizing natural green sources as CDs precursor, such as aloe [2], lemon juice [21]; pericarp [22], orange juice [23], milk protein [24] and plant leaves [25]. There are some projects have been executed in this area, but most of the researchers focused on the application of citric acid-derived CDs and g-C_3N_4 composites for water splitting and organic dye degradation. The reported results are promising but there is still very limited research reported on the use of bioprecursors derived CDs and g-C_3N_4 composite for water remediation application especially for EDC removal. Therefore, few insights are yet to be discovered in this work to fill the gaps of past studies. This includes producing CDs from WH leaves and utilizing sustainable sunlight to irradiate CDs which are more responsive to visible light. In this work, water hyacinth (WH) is chosen as the green source to synthesize CDs using hydrothermal carbonization. WH is considered as the largest invasive aquatic plants due to the reproduces pattern that multiplies its size rapidly and forms dense mats. WH populations have large negative impacts on human society by clogging waterways, wiping out aquatic flora and fauna and forming ideal prerequisite for diseases grow which eventually exacerbating vector-borne diseases. Furthermore, WH also causes important ecological and socio-economic effects [26] and it is considered as one of the world's most damaging and costly species. The aim of our study is to convert WH into valuable CDs via a versatile route and combine CDs with g-C_3N_4 to produce sunlight-responsive composites for photodegradation of 2,4-dichlorophenol.

2 Experimental

2.1 Materials

All the chemical reagents were of analytical grade and used without any further purification. Urea (99.8%, R&M

Chemicals) powder was used to synthesize g-C_3N_4 via pyrolysis method. Milli-Q water was utilized for dilution and washing purpose during the entire experiment. 2,4-dichlorophenol (2,4-DCP, 98.0%, Merck) were used as pollutant model for photocatalytic experiment. In addition, isopropyl alcohol (IPA, 83.5%, QReC), dimethylsulfoxide (DMSO, 99%, Univar), benzoquinone (BQ, 98%, Sigma-Aldrich) and ethylenediamine tetraacetic acid disodium salt (EDTA-2Na^+, 99%, Bio Basic Inc.) were used as scavengers in radical scavenging experiment.

2.2 Preparation of g-C_3N_4

The g-C_3N_4 was synthesized by using a facile thermal heating method. In details, 10 g of urea was placed in a crucible with a cover under ambient pressure and dried in an oven at 80 °C for 12 h. Then the crucible with dried urea was heated in a muffle furnace at 550 °C for 3 h at a heating rate of 10 °C min^{-1} to complete the reaction. The obtained yellow-colored product was washed with nitric acid (0.1 M) and Milli-Q water for 2 times each with centrifugation at 3500 rpm for 10 min to remove any residual alkaline species (e.g. ammonia) absorbed on the sample surface. Finally the washed derivative were dried overnight in an oven at 80 °C, the obtained g-C_3N_4 was well grounded in an agate mortar [27].

2.3 Preparation of carbon dots

CDs were prepared by hydrothermal treatment of water hyacinths (WH) leaves which were obtained from mining lake in Kampar, Perak. First, the WH leaves were dried overnight in the oven to remove the moisture and finely grinded into powder. 5 g of prepared leaves powder were mixed with 120 mL of Milli-Q water and stirred for 30 min to make the mixture homogeneous. After that, the mixture was transferred into the 150 mL Teflon-lined stainless-steel autoclave to undergo hydrothermal treatment process in the oven for 4 h at 200 °C [28]. After heating, the autoclaves were allowed to naturally cool down at room temperature for more than 1 h and the CDs were collected by removing larger particles through centrifugation at 10,000 rpm for 15 min. The upper light yellowish-brown solution containing CDs were obtained and then dried overnight in an oven at 100 °C converted into solid form to measure the weight [11]. After that, the solid CDs were diluted with 1 L Milli-Q water to obtain the concentration (mg/L). Finally, the CDs solution was stored at 4 °C for further characterization and incorporation with g-C_3N_4. The preparation steps are illustrated in Fig. S1.

2.4 Preparation of CDs/g-C_3N_4 Composites

0.6 g of g-C_3N_4 was mixed with 23 mL of CDs solution and vigorously stirred for 24 h at room temperature to obtain a homogeneous suspension. After that, the mixture was shifted into a 100 mL Teflon-lined stainless steel autoclave and heated for 2 h at 100 °C. Then the autoclave was cooled down naturally for 1 h and the obtained products were washed and collected by centrifugation. The washed sample was then dried overnight at 80 °C. CDs/g-C_3N_4 composite with different weight percentage of CDs (0.6 wt.%, 20 wt.% and 40 wt.%) was synthesized using the same procedures stated above. The synthesized composites were indicated as 0.6CDs/g-C_3N_4, 20CDs/g-C_3N_4 and 40CDs/g-C_3N_4, respectively.

2.5 Characterization

The morphology and composition of CDs/g-C_3N_4 were observed using a field emission scanning electron microscope (FESEM, Auriga, Zeiss) equipped with an energy dispersive X-ray spectroscopy (EDS). The images were obtained at an accelerating voltage of 20 kV. High resolution transmission electron microscope (HRTEM, Tecnai 20, Philips) images were obtained at 200 kV. The crystalline phase was identified using an X-ray diffractometer (XRD, D8 Advance, Bruker). The target used in the diffractometer is copper (Cu Kα radiation, λ = 1.54 Å). The surface chemical composition of samples was analyzed by X-ray photoelectron spectroscopy (XPS, Axis Ultra DLD, Kratos) with Al Kα radiation source. The Fourier transform infrared (FTIR) spectra of products were obtained on a Perkin Elmer Spectrum 400 spectrophotometer at the range of 400–4000 cm^{-1}. Ultraviolet–visible diffuse reflectance spectra (UV–vis DRS) were performed using UV–vis NIR spectrophotometer (UV-260, SHIMADZU) with a wavelength range of 200–800 nm. Brunauer–Emmett–Teller (BET) surface area was based on nitrogen adsorption–desorption isotherms with TriStar II 3020 (Micrometrics®, USA). Photoluminescence (PL) spectra of CDs solution were acquired with a PL spectrophotometer (Perkin Elmer LS 55). An Edinburgh FLS 920 Time Resolved Photoluminescence (TRPL) was used to acquire TRPL spectrum and exciton decay lifetime of x-FZNR/P3HT active layers were obtained using a 376.4 nm picosecond pulsed laser as the excitation source with excitation wavelength 480 nm. The average lifetime, τ of the excited charge-carrier was calculated using the equation below:

$$\tau = \left(B_1T_1^2 + B_2T_2^2 + B_3T_3^2\right)/\left(B_1T_1 + B_2T_2 + B_3T_3\right) \quad (1)$$

2.6 Photocatalytic experiments

The photodegradation of 2,4-DCP was carried out in a 500 mL beaker with the working volume of 200 mL 2,4-DCP solution (5 mg/L). 0.1 g of the prepared 0.6CDs/g-C_3N_4, 20CDs/g-C_3N_4 and 40CDs/g-C_3N_4 composites were loaded in 2,4-DCP solution. A pre-experiment was carried out in dark condition for more than 12 h to acheive the adsorption–desorption equilibrium. The 2,4-DCP samples were analyzed every 15 min using the same HPLC equipment mentioned above. The mobile phase was acetonitrile (ACN) and water in the ratio 80:20 with a flow rate of 0.8 mL/min. An UV detector was used to quantify 2,4-DCP with an analytical wavelength 280 nm. The retention time was found to be 0.25 min. The photocatalytic experiment was executed under clear sky condition at Universiti Tunku Abdul Rahman, Perak, (longitude 4.3394° N and latitude 101.1398° E) between 11.00 am and 2.00 pm from June to September 2019. Sunlight light intensity was dignified using Light meter HS1010A of 2000 × 100 lx and the average light intensity over the duration was found to be 104,000 lx. Table S1 showed the recorded light intensity during the photodegradation.

2.7 Near infrared (NIR) degradation test

40CDs/g-C_3N_4 was adopted as the representative photocatalyst to evaluate the photocatalytic performance under NIR illumination. This is to investigate the contribution of CDs towards NIR-driven photocatalysis. Similar experiment procedure in photocatalytic experiment was repeated with the additional placement of NIR filter glass (λ = 730 nm) on top of the beaker. The surrounding of beaker was covered by aluminum foil to prevent the solution absorbing UV and visible light. The light intensity during the photodegradation was recorded in Table S2.

2.8 Scavenger TEst

A radical scavenger experiment was executed to detect the core reactive radical species associated in the photodegradation of 2,4-DCP. The scavenging experiment was carried out by adding 2 mM dimethylsulfoxide (DMSO) which served as electron (e^-) scavenger. This experiment was repeated by adding 2 mM ethylenediamine tetraacetic acid disodium salt (EDTA-2Na^+), benzoquinone (BQ) and isopropyl alcohol (IPA) which acted as hole (h^+) scavenger, superoxide radical ($^{\bullet}O_2^-$) scavenger and hydroxyl radical ($^{\bullet}OH$) scavenger, respectively. Table S3 shows the recorded light intensity during the radical scavenger experiment.

3 Results and discussion

3.1 Pre-experiment

A pre-experiment was carried out to evaluate the dosing range of CDs. Initially, the concentration of CDs was varied in the range of 0.6, 0.8 and 1.0 wt.%. As shown in Fig. S2, the degradation rate was almost the same among the composites which achieved 80% removal efficiency within 120 min while the degradation rate of pure g-C_3N_4 was 71.3%. The low dosage of CDs did not yield significant contribution to the improvement of degradation efficiency. From the results of pre-experiment, it was found that the optimum dosage trip at higher order and hence the aforementioned range was further moved to 20 and 40 wt.% to study the significance of different weight percentage of CDs for the removal of 2,4-DCP. The incorporation of higher dosage CDs into g-C_3N_4 could improve the degradation efficiency towards the 2,4-DCP and thus the CDs dosage was varied at range 0.6, 20 and 40 wt.%.

3.2 Morphological structure and BET surface area

The morphological structure of g-C_3N_4 and CDs/g-C_3N_4 composites were determined by FESEM analysis. Figure 1a shows the agglomeration and irregular morphology with lamellar structure of g-C_3N_4 while the surface of CDs/g-C_3N_4 composites were more wrinkled and more porous with the increasing concentration of CDs as shown in Fig. 1b–d. A more packed and agglomerated morphological structure was observed after incorporating a lower concentration of CDs (0.6 wt.%) into g-C_3N_4. This is due to the self-assembly process occurred during the hydrothermal treatment [29]. When the concentration of CDs increased to higher range (20 and 40 wt.%), the CDs/g-C_3N_4 composites displayed a loosen morphological structure. This suggests that the increasing concentration of CDs can lower the clustering effect. The EDX was used to detect the elements of the CDs/g-C_3N_4 composites. The existence of bulk g-C_3N_4 and CDs was confirmed by the detection of carbon (C), nitrogen (N) and oxygen (O) as shown in inset of Fig. 1b. The low concentration of O element was detected because of the oxygen reacted with g-C_3N_4 during the pyrolysis process. Figure 1e, f show the TEM and HRTEM image of 0.6CDs/g-C_3N_4, respectively. The small dark spots were observed which indicated that the CDs were uniformly distributed onto the surface of g-C_3N_4. Figure 1f further reveals the presence of CDs with the lattice fringes of 0.213 nm which correspond with to (1 0 0) in-plane lattice spacing

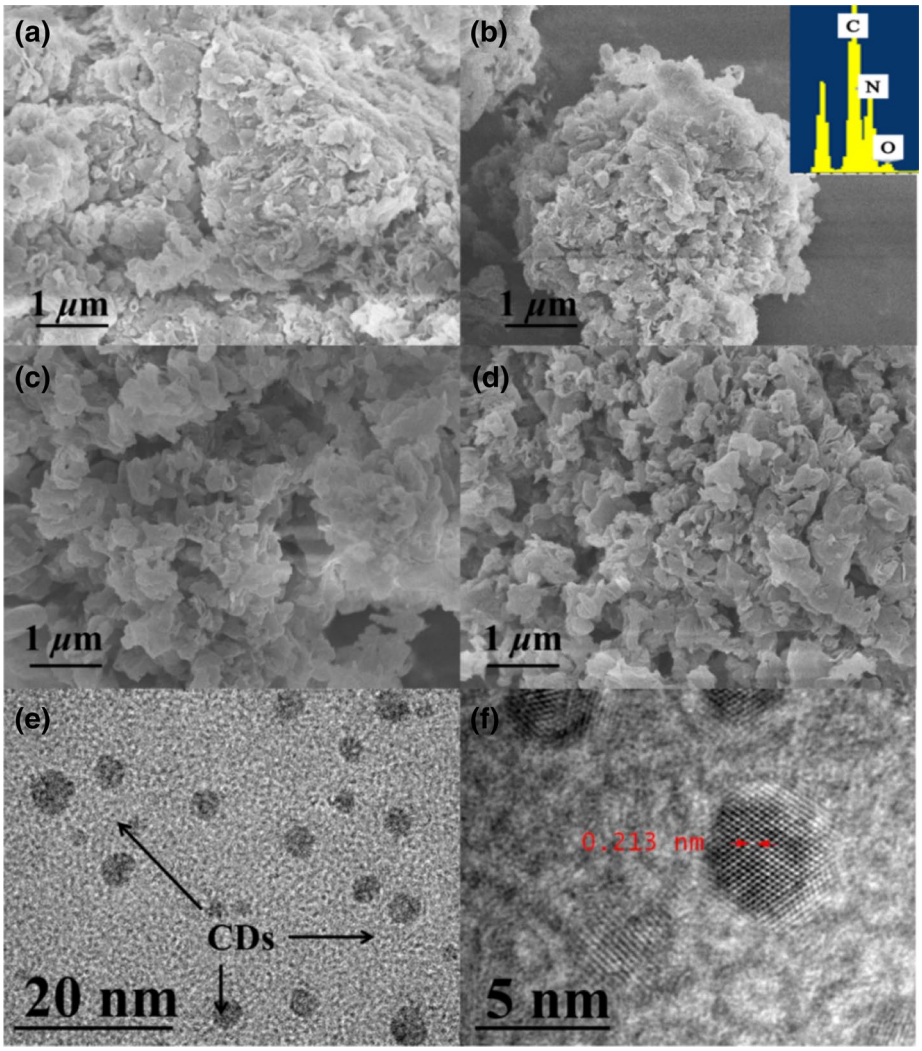

Fig. 1 FESEM images of **a** g-C_3N_4 **b** 0.6CD/g-C_3N_4 **c** 20CD/g-C_3N_4 and **d** 40CD/g-C_3N_4 composites **e** TEM image **f** HRTEM image of 0.6CD/g-C_3N_4. The inset of **b** shows the energy-dispersive X-ray spectroscopy (EDS) results of 0.6CD/g-C_3N_4

Table 1 BET surface area of the prepared samples

Sample	BET Surface Area (m^2/g)	Bandgap Energy (eV)
g-C_3N_4	77.42	2.95
0.6CDs/g-C_3N_4	76.45	2.94
20CDs/g-C_3N_4	65.07	2.92
40CDs/g-C_3N_4	168.98	2.92

of graphene [7, 14, 22]. From Fig. S3, the average particle size of the CDs was found to be 3.1 nm. The particle size ranged from 1.2 nm to 4.9 nm, proving that the nano-sized CDs were successfully prepared. Table 1 shows the BET surface area of as-prepared samples. The BET specific surface area of g-C_3N_4, 0.6CDs/g-C_3N_4, 20CDs/g-C_3N_4 and 40CDs/g-C_3N_4 were 77, 76, 65 and 159 m^2/g, respectively. The 40CDs/g-C_3N_4 composite shows the largest specific surface area among the samples. Theoretically it will enhance the photocatalytic activity since the large specific surface area in heterojunction could increase the number of active sites [30]. These results correlated well with the FESEM results in which the clustering effect occurred at lower concentration of CDs while loosen structure was observed at higher concentration of CDs.

3.3 XRD and FTIR analysis

XRD patterns of CDs and all CDs/g-C_3N_4 composites were presented in Fig. 2a. The two obvious diffraction peaks were found in all composites indexed to the crystal structure of pristine g-C_3N_4. The strong peak at 27° indexed as (0 0 2) was ascribed to the interlayer stacking of aromatic segments with interplanar distance of 0.32 nm. The weak diffraction peak at 12.8° indexed as (1 0 0) corresponded to in-plane structural packing motif of tri-s-triazine [31]. After incorporating 20 and 40 wt.% of CDs into the g-C_3N_4, the diffraction peak shifted from 27.6° to 27.9° because the crystal lattice of g-C_3N_4 distorted with high loading of CDs. This indicates the CDs were successfully intercalated

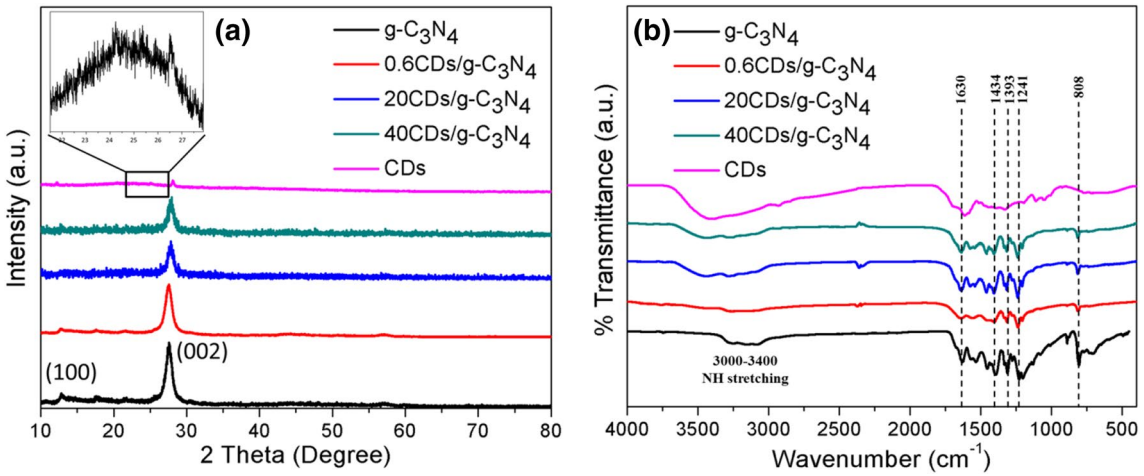

Fig. 2 **a** The XRD patterns and **b** FTIR spectra of CDs, g-C_3N_4, 0.6CD/g-C_3N_4, 20CD/g-C_3N_4 and 40CD/g-C_3N_4. The inset of **a** shows the enlarged XRD pattern of CDs

into the matrix instead of being dispersed on the surface of g-C_3N_4 [32]. However, the low concentration of CDs in 0.6CDs/g-C_3N_4 did not exert notable alteration to the host structure. The intensity of both diffraction peaks at 12.8° and 27° decreased with the increasing loading amount of CDs. This reveals that the existence of CDs inhibited the polymerization of dicyandiamide and the stacking (crystallization) of g-C_3N_4 sheets [32]. The diffraction peaks of CDs were not captured in all composites because the diffraction peak at around 27° was similar to the characteristic diffraction peak of graphite planes (0 0 2) [33]. The inset of Fig. 2a shows a broad (0 0 2) diffraction peak of the CDs at 25° which was attributed to highly disordered carbon atoms and graphitic structure, conforming the amorphous character and graphite-like structure of the CDs [25].

The functional groups in the CDs and composites were identified by using FTIR spectroscopy and shown in Fig. 2b. For the CDs, a broad peak observed at around 3400 cm^{-1} was accredited to the stretching vibration mode of O–H, while a small peak at 2932 cm^{-1} corresponded to the stretching vibration mode of C–H. The band at 1616 cm^{-1} corresponded to C=O stretching of carbonyl groups. Both of vibrational bands at 1052 and 1112 cm^{-1} were credited to the stretching vibrations of C–O–C. Comparable results were also achieved by other researchers [23, 34]. For g-C_3N_4, several absorption peaks observed between the range of 1241 cm^{-1} and 1630 cm^{-1} were assigned to the stretching of sp^3 C–N, and sp^2 C=N that corresponded to the characteristic stretching modes of CN heterocycles [35]. The sharp peak at 808 cm^{-1} was ascribed to the breathing mode of triazine units of g-C_3N_4 [34]. The intensity of these characteristic bands is lower in all composites due to the loading of CDs over the g-C_3N_4. Specifically, the stretching mode of CN heterocycles of g-C_3N_4 exhibited a slight blue-shift from 1241 cm^{-1} to 1238 cm^{-1} with the increasing loading of CDs up 40 wt.%. This may be related to the strengthening of C–N or C=N bond due to the bonding between C atoms of CDs with N atoms of g-C_3N_4 in the composites or some interactions occurred between CDs and g-C_3N_4. The wide peaks in the range of 3000–3400 cm^{-1} were assigned to the stretching vibration modes of N–H and O–H of g-C_3N_4 [36]. Similar CN heterocycles and triazine units of g-C_3N_4 absorption peak were detected for all CD/g-C_3N_4 composites as a result of the low CDs loading amount. The strong absorptions peak of g-C_3N_4 covered the weak absorptions of CDs.

3.4 XPS and absorption spectrum

The chemical state and chemical composition of 0.6CDs/g-C_3N_4 were studied by XPS. Figure 3 shows the narrow scan of XPS spectra and confirmed the existence of C, N and O in the composite. From Fig. 3a, the C1s peak was deconvoluted into three peaks at 284.77 eV, 287.97 eV and 288.83 eV which corresponded to graphitic carbon (C–C), carbonyl (C=O) and sp^2 carbon (N–C=N) [34]. For the N1s spectrum in Fig. 3(b), the main peak observed at 398.51 eV was ascribed to CN=C coordination which originated from the sp^2-bonded N in triazine rings. Meanwhile the other two weak peaks detected at binding energy of 399.80 eV and 400.77 eV were ascribed to tertiary (N–$(C)_3$) and amino functional groups (C–N–H) [36]. The only O 1s peak at 531.91 eV was ascribed to the absorbed water (Fig. 3c) [31].

The optical properties of water hyacinth (WH) derived CDs solution was investigated by UV–Vis absorption and photoluminescence spectrophotometer. Figure 3d shows the UV–vis absorptions of aqueous CDs was in the range between 200 nm and 800 nm. The noticeable peak at

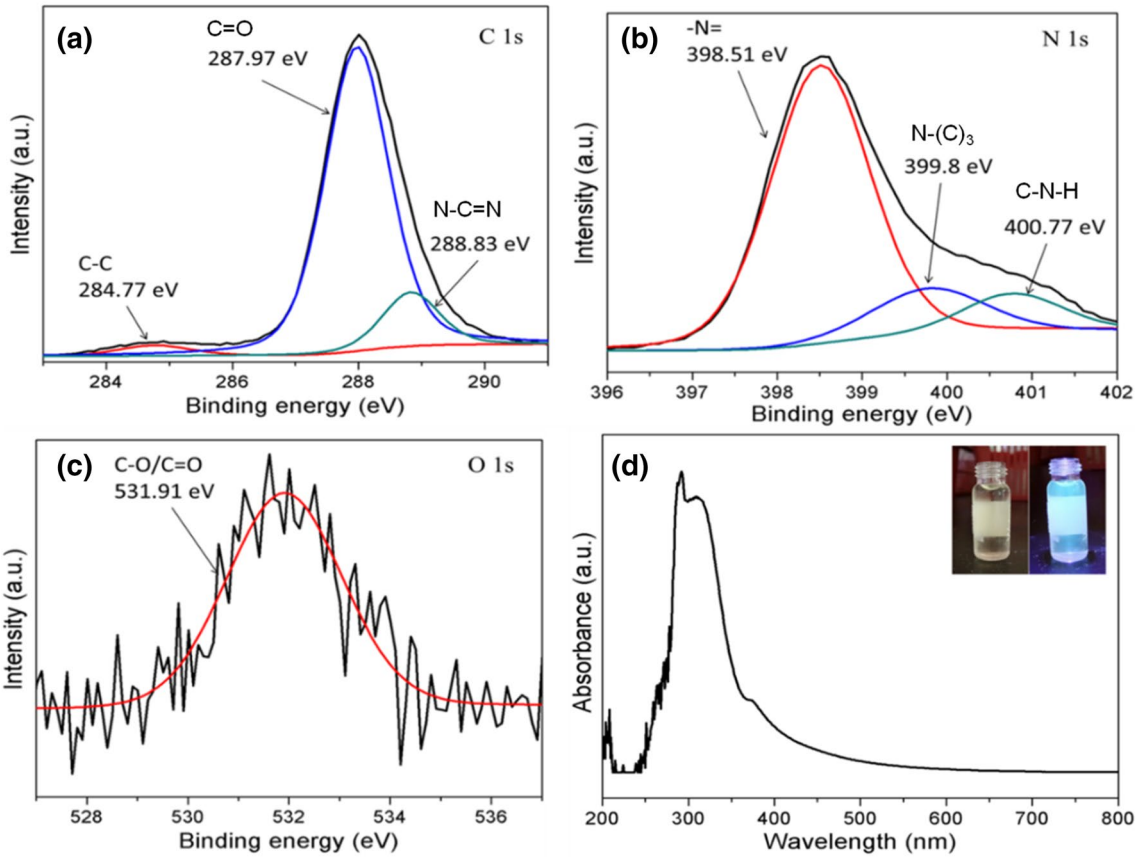

Fig. 3 **a** XPS spectra of 0.6CDs/g-C_3N_4 **a** C1s **b** N1s **c** O1s and **d** The absorption spectrum of CDs solution. Inset of d shows fluorescence of CDs under daylight (left) and UV light irradiation at 365 nm (right)

300 nm was attributed to the n-π* transitions of C=O and π–π* transition of C=C [2]. The inset of Fig. 3d shows the optical properties of synthesized CDs solution, a blue-green fluorescence was emitted upon irradiation by UV light at 365 nm.

3.5 TRPL and UV–vis DRS analysis

The excitation-dependent PL spectra of WH derived CDs solution is shown in Fig. 4a. The ideal spectrum that induced the PL properties of CDs solution was studied by varying the excitation wavelength from 320 to 540 nm. The fluorescence emission of CDs exhibited a wide peak from the UV (380 nm) to visible spectrum (500 nm). The CDs showed a strong emission peak when excited by the light with wavelength from 320 to 380 nm. The emission spectrum was red-shifted with decreasing intensity as the excitation wavelength increased from 400 to 540 nm. No significance emission peak was observed when the excitation wavelength exceeded 540 nm. This means that the synthesized CDs did not acquire the upconverted photoluminescence (UCPL) properties that could convert the absorbed NIR light to shorter wavelength for the occurrence of electron excitation at low energy input. The foundation of the photoluminescence properties of CDs is not completely understood but they are normally influenced by the size distribution of CDs, structure of nanoparticles and different distribution of emissive traps sites [3]. From the previous researches, there are limited report on CDs and graphene quantum dots (GQDs) that acquired UCPL properties. Some researchers denied the UCPL properties of CDs [37, 38] and claimed that the regularly cited UCPL properties might initiate from the standard fluorescence excited by the leaking component in the monochromater of the fluorescence spectrophotometer [39].

The light absorption properties of the synthesized samples were determined by UV–vis DRS analysis in Fig. 4b. The absorption peaks of all CDs/g-C_3N_4 composites red shifted towards higher wavelength in visible and NIR region. When the concentration of CDs increased, the intensity of shoulder peak also increased and the absorption edge gradually red shifted towards longer wavelength. The shoulder peak was triggered by the light absorption of CDs and the red shift of absorption edge

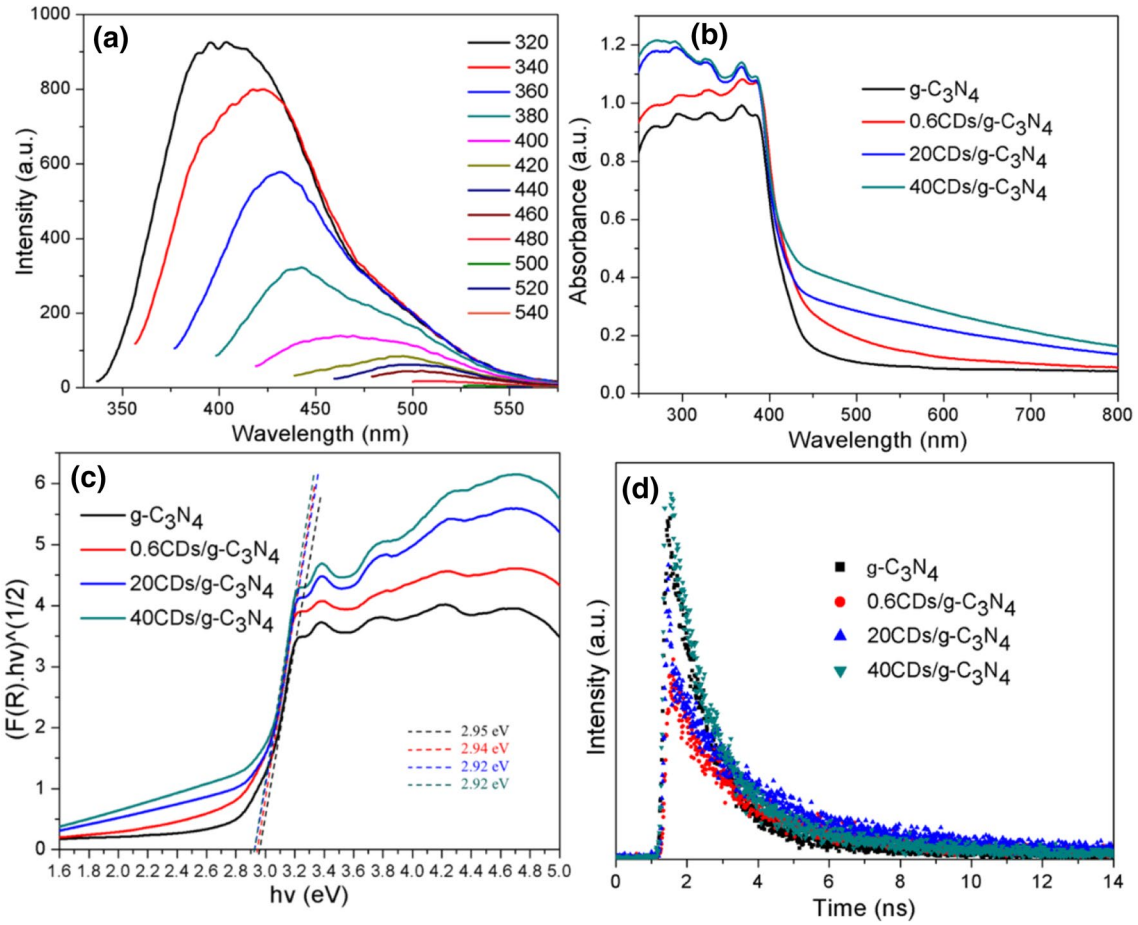

Fig. 4 **a** The emission wavelength of CDs solution at different excitation spectrum, **b** UV–visible diffuse reflectance spectra, **c** Tauc plots and **d** TRPL spectrum of g-C_3N_4, 0.6CDs/g-C_3N_4, 20CDs/g-C_3N_4 and 40CDs/g-C_3N_4

was attributable to the interfacial interaction between the CDs and g-C_3N_4 [34]. Although it is proved that CDs were able to absorb NIR light, the photon energy of NIR light is too low to induce photoexcitation. In this context, CDs played a vital role to sensitize g-C_3N_4 to harvest more visible light instead of NIR light to excite more electrons for the improvement of photocatalytic performance.

The band gap energy was obtained through the Tauc plot (Fig. 4c). It was determined by plotting $(F(R).\ h\nu)^{1/2}$ against hν, where Kubelka–Munk function F(R) is derived from following equation [40]:

$$F(R) = (1 - R)^2/2R \tag{2}$$

where hν is the photon energy and R is diffuse reflectance. Figure 4d shows the interception of the tangent of each curve to the photon energy (x-axis) to determine the band gap energy of the synthesized samples. The obtained band gap energy was corresponded to the optical shift in Fig. 4b, where the lower shift had a wider band gap while the higher shift toward the visible light region obtained a narrower band gap. As shown in Table 1, the band gap energy of g-C_3N_4 (2.95 eV) decreased significantly from 2.95 eV to 2.92 eV after modifying with CDs at higher percentage.

Time-resolved PL (TRPL) spectra shown in Fig. 4d were adopted to study the dynamic electron transfer process of the samples. In general, the longer lifetime is credited to an effective electron–hole pairs separation, while the shorter lifetime is attributed to the rapid recombination of the electron–hole pairs. Table S4 shows all the fitted parameters. The charge-carrier lifetimes of these composites increased in the following order: g-C_3N_4 < 40CDs/g-C_3N_4 < 0.6CDs/g-C_3N_4 < 20CDs/g-C_3N_4. Among the samples, 20CDs/g-C_3N_4 exhibited the longest charge-carrier lifetime with 4.897 ns while g-C_3N_4 possessed the shortest charge carrier lifetime of 1.724 ns. This reveals that the 20CDs/g-C_3N_4 achieved the highest electron–hole pairs separation efficiency compared to the others. When the CDs were incorporated into g-C_3N_4, CDs could function as the reservoir to trap the excited electron due to the surface junction between both semiconductors that

could enhance the separation of electron–hole pairs. This could result in the enhancement of photocatalytic activity because more electrons and holes will involve in the redox reactions to produce strong oxidizing agents for the degradation of targeted pollutant. However, the highest dosage of CDs in 40CDs/g-C_3N_4 increased the electron–hole pairs recombination. The enlargement of CDs coverage formed the trap states at the interface between CDs and g-C_3N_4, and thus fewer electrons fill in the interfacial trap states. This could lead to the increase of trapping events and decelerate the electron transport [41]. A similar observation was reported by Fang and co-workers. They claimed that excessive dosage of CDs will act as recombination centers and lower down the electron–hole pairs separation efficiency [32].

3.6 Photocatalytic performance

The photocatalytic performances of pure g-C_3N_4 and different wt.% CDs/g-C_3N_4 composites were evaluated by degrading 2,4-DCP under natural sunlight irradiation. Prior to the photodegradation under sunlight, the 2,4-DCP solution was stirred in the dark condition for 18 h to form adsorption–desorption equilibrium. The 2,4-DCP concentration reduced approximately 20% for all samples when the adsorption–desorption equilibrium was established. The photodegradation rate was calculated using the following equation:

$$\text{Photodegradation rate} = \left(\frac{C_0 - C}{C_0}\right) \times 100\% \quad (3)$$

where C_0 and C are the 2,4-DCP concentrations in the solution at time 0 and t min, respectively.

Table 2 summarizes the correlation between the physicochemical properties of photocatalyst and their degradation performance. There was no degradation occurred throughout the experiment in the blank sample as shown in Fig. 5a, indicating that the 2,4-DCP was a poor photosensitizing compound and the degradation was purely performed by the applied photocatalysts. The 2,4-DCP was almost fully degraded by 20CDs/g-C_3N_4 and 40CDs/g-C_3N_4 within 120 min with similar removal efficiency of 94%. While the removal efficiency of 0.6CDs/g-C_3N_4 and g-C_3N_4 was 79.63% and 71.30%, respectively (Table 2). The low band gap of pure g-C_3N_4 (2.95 eV) caused a moderately good photodegradation of BPA. The degradation efficiency increased ~ 14% from 0.6CDs/g-C_3N_4 to 20CDs/g-C_3N_4 composite, suggesting that high loading of CDs can boost the degradation efficiency. Fig. S4 shows the first order kinetic model of 2,4-DCP degradation process and the rate constant, k value of g-C_3N_4, 0.6CDs/g-C_3N_4, 20CDs/g-C_3N_4 and 40CDs/g-C_3N_4 were 0.011, 0.013, 0.0194, and 0.0186 min^{-1} respectively (Fig. 5b).

Among the samples, both of 20CDs/g-C_3N_4 and 40CDs/g-C_3N_4 achieved the highest degradation rate of 94% which was 1.76 times higher than that of g-C_3N_4. The superior degradation efficiency of 20CDs/g-C_3N_4 was predominantly due to the prolonged lifetime of electron–hole pairs in the composites which correlated well with the TRPL results (Table S4). The prolonged charge-carrier lifetime promoted more holes and electrons to react with water and oxygen to produce more hydroxyl and superoxide anion radicals for the degradation of 2,4-DCP. Although 40CDs/g-C_3N_4 showed shorter charge-carrier lifetime than 0.6CDs/g-C_3N_4 and 20CDs/g-C_3N_4, the degradation rate was higher than 0.6CDs/g-C_3N_4 and similar with 20CDs/g-C_3N_4. These results advocated that the excellent light harvesting ability and high surface area of 40CDs/g-C_3N_4 could overcome the limitation of short charge carrier lifetime and achieved similar degradation efficiency with 20CDs/g-C_3N_4. Thus it is concluded that both of the electron–hole pairs separation efficiency and extension of light absorption spectrum were equally important for the improvement of photocatalytic performance. Meanwhile the increased surface area of the composites could supply extra active sites for the degradation of 2,4-DCP. These factors played an essential role to improve the overall degradation efficiency.

20CDs/g-C_3N_4 composite was chosen to determine the active species in scavenging experiment due to their excellent performance with optimum amount of CDs. Several types of scavengers were used in this experiment such as ethylene diamine-tetraacetic acid disodium salt (EDTA-2Na^+), benzoquinone (BQ), isopropyl alcohol (IPA) and dimethyl sulfoxide (DMSO) which worked as holes

Table 2 Correlation between physicochemical properties and degradation performance

Photocatalyst	Physicochemical properties			
	BET surface area	Visible light absorption	Charge carriers lifetime	2,4-DCP degradation efficiency (%)
g-C_3N_4	Moderate	Lowest	Shortest	71.30
0.6CDs/g-C_3N_4	Moderate	Low	Moderate	79.63
20CDs/g-C_3N_4	Small	Moderate	Long	93.77
40CDs/g-C_3N_4	Large	High	Short	94.00

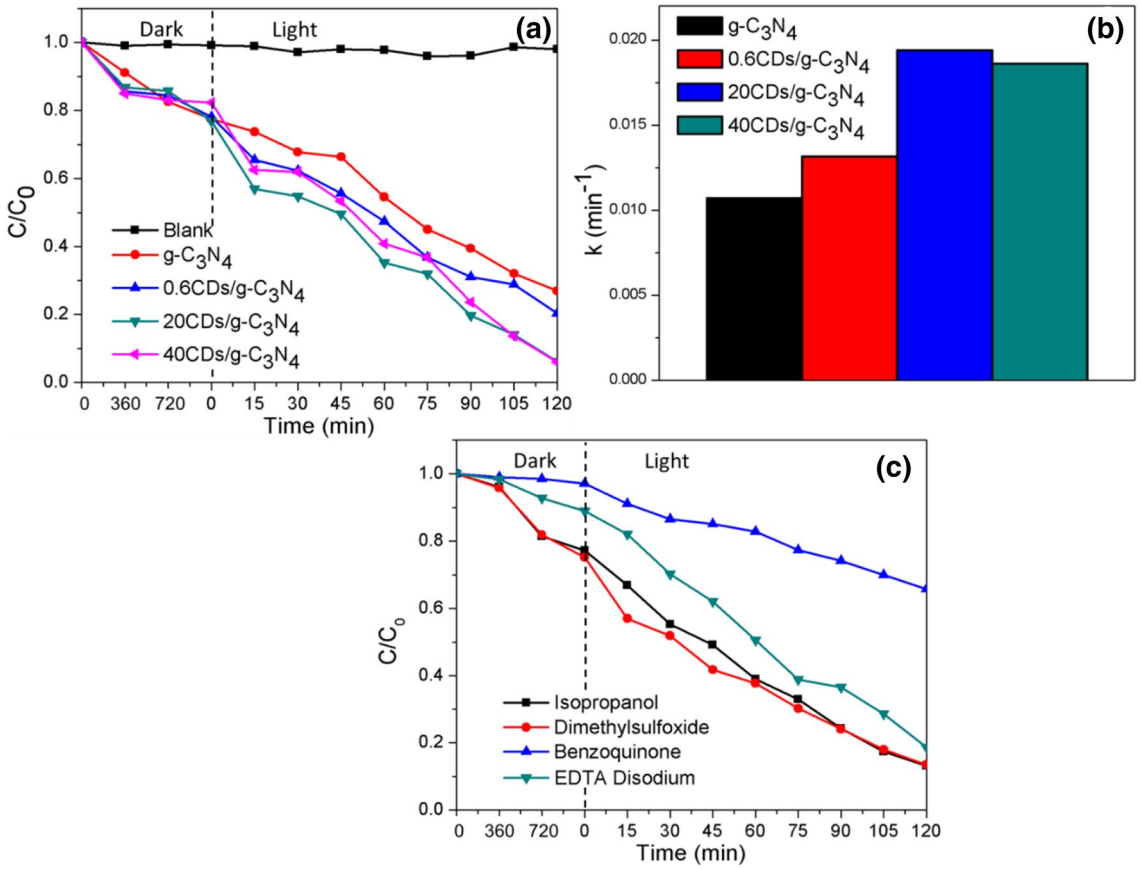

Fig. 5 **a** Photocatalytic degradation of 2,4-DCP, **b** Apparent rate constant, k of the samples and **c** Scavengers test results of CDs/g-C_3N_4

(h^+), superoxide radicals ($^{\cdot}O_2^-$), hydroxyl radicals ($^{\bullet}$OH) and electron (e^-) catcher, respectively [42]. Figure 5c displays the degradation rate in the order of DMSO > IPA > EDTA-2Na^+ > BQ. The low degradation efficiency indicated that the active species was being captured by scavenger and unable to perform degradation. Both of the e^- and $^{\cdot}$OH were not the active species in the photodegradation of 2,4-DCP since the degradation in DMSO and IPA did not show significant changes. Upon the addition of BQ in the 2,4-DCP, the degradation rate was highly suppressed [43]. This shows that $^{\cdot}O_2^-$ was one of the main active species involved in the photodegradation process. The addition of EDTA-2Na^+ slightly inhibited the degradation rate, indicating that the h^+ was the second active species.

The edge potential of the valence band (VB) and the conduction band (CB) of a photocatalyst at the point of zero charge were projected by using equations below:

$$E_{VB} = X - E_c + 0.5E_g \quad (4)$$

$$E_{CB} = E_{VB} - E_g \quad (5)$$

where E_{CB} and E_{VB} are the CB and VB edge potential respectively, E_g is the band gap energy of the semiconductor.; E_c is the energy of free electrons on the hydrogen scale (≈4.5 eV vs NHE) and X is the electronegativity of the semiconductor The X value of g-C_3N_4 is 4.64 eV [44] while the band gap energy of g-C_3N_4 is 2.95 eV (Table 1). The VB and CB of g-C_3N_4 were calculated to be 1.62 eV and −1.33 eV, respectively. Figure 6 illustrated the schematic diagram of degradation mechanism of CDs/g-C_3N_4 composite. When the g-C_3N_4 was irradiated under the natural sunlight, the electrons in the VB were excited to the CB of g-C_3N_4 to form electron–hole pairs. The holes (h^+) in the VB of g-C_3N_4 directly oxidized 2,4-DCP but could not react with water (H_2O) and hydroxide (OH^-) to form $^{\bullet}$OH radical. This is due to the VB of g-C_3N_4 (+1.62 eV) was less positive than the standard redox potential of $OH^-/^{\bullet}OH$ (+1.99 eV vs. NHE) and $H_2O/^{\bullet}OH$ (+2.38 eV vs. NHE) [45]. Simultaneously, when CDs was incorporated into g-C_3N_4, the CDs acted as electron acceptors to trap the excited electron (e^-) from CB of g-C_3N_4 due to their conducting texture and excellent charge storing ability (Fig. 6a). This helps to stimulate the separation and prolonging the lifetime of electron–hole pairs. The electrons will further react

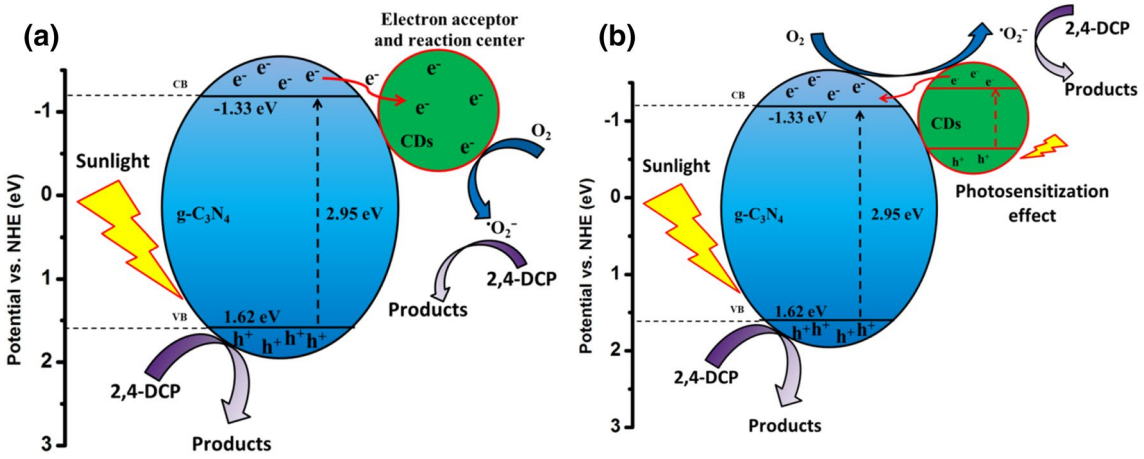

Fig. 6 Photocatalysis mechanism of CDs/g-C_3N_4 **a** As an electron acceptor and reaction center **b** photosensitization effect of CDs

with the dissolved oxygen to form superoxide ($^{\cdot}O_2^-$) anion radicals to oxidize the 2,4-DCP. Furthermore, the photosensitizing effect of CDs can convert the photon energy to excite electron to sensitize g-C_3N_4 and donate the electrons to the CB of g-C_3N_4 (Fig. 6b) [46]. Subsequently the visible light response range of the synthesized samples were used for the photocatalytic degradation of 2,4-DCP. The π-conjugated of CDs function as a photosensitizer to sensitize g-C_3N_4 and introduce more photoexcited electrons to the CB of g-C_3N_4 [14]. However, as the result of 2,4-DCP degradation efficiency was well in line with the TRPL results, the photogenerated electron–hole pairs separation efficiency worked as the prevailing factor for the advancement of photocatalytic performance in CDs/g-C_3N_4 composites. Zhang et al. (2015) and Wang et al. (2013) reported that heterojunction interface between CDs and g-C_3N_4 efficiently promoted the rapid interfacial charge transfer and thus enhancing the electron–hole pairs separation [7, 20]. This occasioned in the generation of more electrons and holes to produce more active radicals like $^{\cdot}OH$ and $^{\cdot}O_2^-$ for the removal of targeted pollutant.

In order to understand the NIR-driven ability of synthesized CDs/g-C_3N_4 composite, 40CDs/g-C_3N_4 was chosen to evaluate the photocatalytic performance under near infrared (NIR) illumination due to the outstanding absorption ability compared to other prepared composites. Fig. S5 shows the results of NIR degradation test, which the degradation efficiency of 40CDs/g-C_3N_4 was 23% after 120 min under IR irradiation. The degradation efficiency is extremely low compared with the result under sunlight irradiation (94%). This result further confirms that photoexcitation of a photocatalyst could not occur under the irradiation of NIR light and hence the removal of targeted pollutant was not significant.

Table 3 shows the comparison study results between the present study and previous literature report. In this present study, the CDs/g-C_3N_4 was able to degrade 94.0% of 2,4-DCP within 120 min while the CDs/g-C_3N_4 composite synthesized by Zhang et al. [13] managed to fully degrade phenol compound within 200 min. This suggests that phenol compound need longer duration for the complete degradation. Furthermore, most of the reported CDs composites such as CDs/g-C_3N_4, CDs/Bi_2WO_6 and CDs/BiOI fully degrade BPA within 120 min due to high photogenerated electron–hole pairs separation rate and extended light absorption range [47, 48]. Di and co-workers reported that nitrogen doped carbon dots (N-CDs) were capable to facilitate the superior activation of molecular oxygen, resulted in superior 4-chlorophenol (4-CP) removal efficiency in N-CDs/$BiPO_4$ composite [49]. Overall, the

Table 3 Comparison study of the degradation of EDCs using other photocatalysts

Composite	Pollutant	Catalyst (mg)	Initial concentration (mg/L)	Duration (min)	Degradation efficiency, %	References
CDs/g-C_3N_4	2,4-DCP	100	5	120	94.0	Present study
CDs/g-C_3N_4	Phenol	50	10	200	100.0	[13]
CDs/Bi_2WO_6	BPA	100	10	60	100.0	[45]
CDs/BiOI	BPA	100	10	120	100.0	[46]
N-CDs/$BiPO_4$	4-CP	30	10	120	100.0	[47]

degradation results of the present study are comparable with previous works which reported the use of citric acid to produce CDs [13, 46]. The CDs was derived from plant wastes which is water hyacinth instead of chemicals, thus a sustainable and greener solution for environmental remediation is produced.

4 Conclusion

CDs were successfully derived from WH leaves via a green and versatile route and the CDs/g-C_3N_4 composites were successfully amalgamated via hydrothermal treatment. The particle size of CDs ranged from 1.2 nm to 4.9 nm and a blue-green fluorescence was emitted under the UV light irradiation at 365 nm. After incorporating CDs into the g-C_3N_4, the light respond ranges of CDs/g-C_3N_4 composites shifted towards the visible region and the band gap energy of g-C_3N_4, 0.6CDs/g-C_3N_4, 20CDs/g-C_3N_4 and 40CDs/g-C_3N_4 were measured to be 2.95 eV, 2.94 eV, 2.92 eV and 2.92 eV, respectively. Both of 20CDs/g-C_3N_4 and 40CDs/g-C_3N_4 reached the highest removal efficiency of 94% within 120 min. The removal efficiency of 0.6CDs/g-C_3N_4 and g-C_3N_4 was 79.63% and 71.30%, respectively. The superior electron–hole pairs separation properties of 20CDs/g-C_3N_4 had boosted the photocatalytic performance. While the short charge carrier lifetime of 40CDs/g-C_3N_4 was overcome by its outstanding light harvesting ability and high surface area which helped to generate more electron–hole pairs and supplied more active sites for the adsorption of 2,4-DCP.

Acknowledgements This work was supported by the Fundamental Research Grant Scheme (FRGS/1/2019/TK10/UTAR/02/5) and Universiti Tunku Abdul Rahman Research Fund (IPSR/RMC/UTARRF/2018-C2/L03).

Compliance with ethical standards

Conflict of interest On behalf of all authors, the corresponding author states that there is no conflict of interest.

References

1. Xu X, Ray R, Gu Y, Ploehn HJ, Gearheart L, Raker K, Scrivens WA (2004) Electrophoretic analysis and purification of fluorescent single-walled carbon nanotube fragments. J Am Chem Soc 126:12736–12737. https://doi.org/10.1021/ja040082h
2. Xu H, Yang X, Li G, Zhao C, Liao X (2015) Green synthesis of fluorescent carbon dots for selective detection of tartrazine in food samples. J Agric Food Chem 63:6707–6714. https://doi.org/10.1021/acs.jafc.5b02319
3. Chen W, Hu C, Yang Y, Cui J, Liu Y (2016) Rapid synthesis of carbon dots by hydrothermal treatment of lignin. Materials 9:184. https://doi.org/10.3390/ma9030184
4. Thambiraj S, Shankaran R (2016) Green synthesis of highly fluorescent carbon quantum dots from sugarcane bagasse pulp. Appl Surf Sci 390:435–443. https://doi.org/10.1016/j.apsusc.2016.08.106
5. Wang F, Chen P, Feng Y, Xie Z, Liu Y, Su Y, Zhang Q, Wang Y, Yao K, Lv W, Liu G (2017) Facile synthesis of N-doped carbon dots/g-C_3N_4 photocatalyst with enhanced visible-light photocatalytic activity for the degradation of indomethacin. Appl Catal B 207:103–113. https://doi.org/10.1016/j.apcatb.2017.02.024
6. Das R, Bandyopadhyay R, Pramanik P (2018) Carbon quantum dots from natural resource: a review. Mater Today Chem 8:96–109. https://doi.org/10.1016/j.mtchem.2018.03.003
7. Zhang Z, Sun W, Wu P (2015) Highly photoluminescent carbon dots derived from egg white: facile and green synthesis, photoluminescence properties, and multiple applications. ACS Sustain Chem Eng 3:1412–1418. https://doi.org/10.1021/acssuschemeng.5b00156
8. Yue L, Li H, Liu Q, Guo D, Chen J, Sun Q, Xu Y, Wu F (2019) Manganese-doped carbon quantum dots for fluorometric and magnetic resonance (dual mode) bioimaging and biosensing. Microchim Acta 186:315. https://doi.org/10.1007/s00604-019-3407-8
9. Huang C, Dong H, Su Y, Wu Y, Narron R, Yong Q (2019) Synthesis of carbon quantum dot nanoparticles derived from byproducts in bio-refinery process for cell imaging and in vivo bioimaging. Nanomaterials 9:387. https://doi.org/10.3390/nano9030387
10. Song SH, Jang M, Yoon H, Cho YH, Jeon S, Kim BH (2016) Size and pH dependent photoluminescence of graphene quantum dots with low oxygen content. RSC Adv 6:97990–97994. https://doi.org/10.1039/C6RA21651J
11. Tyagi A, Tripathi KM, Singh N, Choudhary S, Gupta RK (2016) Green synthesis of carbon quantum dots from lemon peel waste: applications in sensing and photocatalysis. RSC Adv 6:72423–72432. https://doi.org/10.1039/C6RA10488F
12. Yoo D, Park Y, Cheon B, Park MH (2019) Carbon dots as an effective fluorescent sensing platform for metal ion detection. Nanoscale Res Lett 14:1–3. https://doi.org/10.1186/s11671-019-3088-6
13. Zhang H, Zhao L, Geng F, Guo LH, Wan B, Yang Y (2016) Carbon dots decorated graphitic carbon nitride as an efficient metal-free photocatalyst for phenol degradation. Appl Catal B 180:656–662. https://doi.org/10.1016/j.apcatb.2015.06.056
14. Li K, Su FY, Zhang WD (2016) Modification of g-C_3N_4 nanosheets by carbon quantum dots for highly efficient photocatalytic generation of hydrogen. Appl Surf Sci 375:110–117. https://doi.org/10.1016/j.apsusc.2016.03.025
15. Ke J, Li X, Zhao Q, Liu B, Liu S, Wang S (2017) Upconversion carbon quantum dots as visible light responsive component for efficient enhancement of photocatalytic performance. J Colloid Interface Sci 496:425–433. https://doi.org/10.1016/j.jcis.2017.01.121
16. Yu BY, Kwak SY (2012) Carbon quantum dots embedded with mesoporous hematite nanospheres as efficient visible light-active photocatalysts. J Mater Chem 22:8345–8353. https://doi.org/10.1039/C2JM16931BB
17. Zhang H, Ming H, Lian S, Huang H, Li H, Zhang L, Liu Y, Kang Z, Lee ST (2011) Fe_2O_3/carbon quantum dots complex photocatalysts and their enhanced photocatalytic activity under visible light. Dalton Trans 40:10822–10825. https://doi.org/10.1039/C1DT11147G
18. Cheng Y, Bai M, Su J, Fang C, Li H, Chen J, Jiao J (2019) Synthesis of fluorescent carbon quantum dots from aqua mesophase pitch and their photocatalytic degradation activity of organic dyes. J Mater Sci Technol 35:1515–1522. https://doi.org/10.1016/j.jmst.2019.03.039
19. He K, Xie J, Liu ZQ, Li N, Chen X, Hu J, Li X (2018) Multi-functional Ni_3C cocatalyst/g-C_3N_4 nanoheterojunctions for robust

photocatalytic H_2 evolution under visible light. J Mater Chem A 6:13110–13122. https://doi.org/10.1039/C8TA03048K
20. Wang Y, Wang Q, Zhan X, Wang F, Safdar M, He J (2013) Visible light driven type II heterostructures and their enhanced photocatalysis properties: a review. Nanoscale 5:8326–8339. https://doi.org/10.1039/C3NR01577G
21. Hoan BT, Tam PD, Pham VH (2019) Green synthesis of highly luminescent carbon quantum dots from lemon juice. J Nanotechnol. https://doi.org/10.1155/2019/2852816
22. Du W, Xu X, Hao H, Liu R, Zhang D, Gao F, Lu Q (2015) Green synthesis of fluorescent carbon quantum dots and carbon spheres from pericarp. Sci China Chem 58:863–870. https://doi.org/10.1007/s11426-014-5256-y
23. Sahu S, Behera B, Maiti TK, Mohapatra S (2012) Simple one-step synthesis of highly luminescent carbon dots from orange juice: application as excellent bio-imaging agents. Chem Commun 48:8835–8837. https://doi.org/10.1039/C2CC33796G
24. Bajpai SK, D'Souza A, Suhail B (2019) Blue light-emitting carbon dots (CDs) from a milk protein and their interaction with Spinacia oleracea leaf cells. Int Nano Lett 9:203–212. https://doi.org/10.1007/s40089-019-0271-9
25. Zhu S, Meng Q, Wang L, Zhang J, Song Y, Jin H, Zhang K, Sun H, Wang H, Yang B (2013) Highly photoluminescent carbon dots for multicolor patterning, sensors, and bioimaging. Angew Chem Int Ed 52:3953–3957. https://doi.org/10.1002/anie.201300519
26. Villamagna AM, Murphy BR (2010) Ecological and socio-economic impacts of invasive water hyacinth (*Eichhornia crassipes*): a review. Freshw Biol 55:282–298. https://doi.org/10.1111/j.1365-2427.2009.02294.x
27. Zhou S, Liu Y, Li J, Wang Y, Jiang G, Zhao Z, Wang D, Duan A, Liu J, Wei Y (2014) Facile in situ synthesis of graphitic carbon nitride (g-C_3N_4)-N-TiO_2 heterojunction as an efficient photocatalyst for the selective photoreduction of CO_2 to CO. Appl Catal B 158:20–29. https://doi.org/10.1016/j.apcatb.2014.03.037
28. Sachdev A, Gopinath P (2015) Green synthesis of multifunctional carbon dots from coriander leaves and their potential application as antioxidants, sensors and bioimaging agents. Analyst 140:4260–4269. https://doi.org/10.1039/C5AN00454C
29. Gao J, Zhou Y, Li Z, Yan S, Wang N, Zou Z (2012) High-yield synthesis of millimetre-long, semiconducting carbon nitride nanotubes with intense photoluminescence emission and reproducible photoconductivity. Nanoscale 4:3687–3692. https://doi.org/10.1039/C2NR30777D
30. Guo Y, Zhang L, Cao F, Leng Y (2016) Thermal treatment of hair for the synthesis of sustainable carbon quantum dots and the applications for sensing Hg^{2+}. Sci Rep 6:35795. https://doi.org/10.1038/srep35795
31. Lu W, Xu T, Wang Y, Hu H, Li N, Jiang X, Chen W (2016) Synergistic photocatalytic properties and mechanism of g-C_3N_4 coupled with zinc phthalocyanine catalyst under visible light irradiation. Appl Catal B 180:20–28. https://doi.org/10.1016/j.apcatb.2015.06.009
32. Fang S, Xia Y, Lv K, Li Q, Sun J, Li M (2016) Effect of carbon-dots modification on the structure and photocatalytic activity of g-C_3N_4. Appl Catal B 185:225–232. https://doi.org/10.1016/j.apcatb.2015.12.025
33. Das P, Bose M, Ganguly S, Mondal S, Das AK, Banerjee S, Das NC (2017) Green approach to photoluminescent carbon dots for imaging of gram-negative bacteria Escherichia coli. Nanotechnology 28:195501. https://doi.org/10.1088/1361-6528/aa6714
34. Sim LC, Wong JL, Hak CH, Tai JY, Leong KH, Saravanan P (2018) Sugarcane juice derived carbon dot–graphitic carbon nitride composites for bisphenol A degradation under sunlight irradiation. Beilstein J Nanotechnol 9:353–363. https://doi.org/10.3762/bjnano.9.35
35. Jian X, Liu X, Yang HM, Li JG, Song XL, Dai HY, Liang ZH (2016) Construction of carbon quantum dots/proton-functionalized graphitic carbon nitride nanocomposite via electrostatic self-assembly strategy and its application. Appl Surf Sci 370:514–521. https://doi.org/10.1016/j.apsusc.2016.02.119
36. Guo F, Shi W, Guan W, Huang H, Liu Y (2017) Carbon dots/g-C_3N_4/ZnO nanocomposite as efficient visible-light driven photocatalyst for tetracycline total degradation. Sep Purif Technol 173:295–303. https://doi.org/10.1016/j.seppur.2016.09.040
37. Tan D, Zhou S, Qiu J (2012) Comment on "upconversion and downconversion fluorescent graphene quantum dots: ultrasonic preparation and photocatalysis". ACS Nano 6:6530–6531. https://doi.org/10.1021/nn3016822
38. Gan Z, Wu X, Zhou G, Shen J, Chu PK (2013) Is there real upconversion photoluminescence from graphene quantum dots? Adv Opt Mater 1:554–558. https://doi.org/10.1002/adom.201300152
39. Wen X, Yu P, Toh YR, Ma X, Tang J (2014) On the upconversion fluorescence in carbon nanodots and graphene quantum dots. ChemComm 50:4703–4706. https://doi.org/10.1039/C4CC01213E
40. Kubelka P, Munk F (1931) An article on optics of paint layers. Z Tech Phys 12:593–601
41. Maloney F, Poudyal U, Chen W, Wang W (2016) Influence of quantum dot concentration on carrier transport in ZnO: TiO_2 nano-hybrid photoanodes for quantum dot-sensitized solar cells. Nanomaterials 6:191. https://doi.org/10.3390/nano6110191
42. Nayak S, Swain G, Parida K (2019) Enhanced photocatalytic activities of RhB degradation and H_2 evolution from in situ formation of the electrostatic heterostructure MoS_2/NiFe LDH nanocomposite through the Z-scheme mechanism via p–n heterojunctions. ACS Appl Mater Interfaces 11:20923–20942. https://doi.org/10.1021/acsami.9b06511
43. Rajendran R, Varadharajan K, Jayaraman V, Singaram B, Jeyaram J (2018) Photocatalytic degradation of metronidazole and methylene blue by PVA-assisted Bi_2WO_6–CdS nanocomposite film under visible light irradiation. Appl Nanosci 8:61–78. https://doi.org/10.1007/s13204-018-0652-9
44. Leong KH, Chu HY, Ibrahim S, Saravanan P (2015) Palladium nanoparticles anchored to anatase TiO_2 for enhanced surface plasmon resonance-stimulated, visible-light-driven photocatalytic activity. Beilstein J Nanotechnol 6:428–437. https://doi.org/10.3762/bjnano.6.43
45. Ni Z, Dong F, Huang H, Zhang Y (2016) New insights into how Pd nanoparticles influence the photocatalytic oxidation and reduction ability of g-C_3N_4 nanosheets. Catal Sci Technol 6:6448–6458. https://doi.org/10.1039/C6CY00580B
46. Liu Q, Chen T, Guo Y, Zhang Z, Fang X (2016) Ultrathin g-C_3N_4 nanosheets coupled with carbon nanodots as 2D/0D composites for efficient photocatalytic H_2 evolution. Appl Catal B 193:248–258. https://doi.org/10.1016/j.apcatb.2016.04.034
47. Wang J, Tang L, Zeng G, Deng Y, Dong H, Liu Y, Wang L, Peng B, Zhang C, Chen F (2018) 0D/2D interface engineering of carbon quantum dots modified Bi_2WO_6 ultrathin nanosheets with enhanced photoactivity for full spectrum light utilization and mechanism insight. Appl Catal B 222:115–123. https://doi.org/10.1016/j.apcatb.2017.10.014
48. Di J, Xia J, Ji M, Wang B, Yin S, Xu H, Chen Z, Li H (2016) Carbon quantum dots induced ultrasmall BiOI nanosheets with assembled hollow structures for broad spectrum

photocatalytic activity and mechanism insight. Langmuir 32:2075–2084. https://doi.org/10.1021/acs.langmuir.5b04308
49. Di J, Xia J, Chen X, Ji M, Yin S, Zhang Q, Li H (2017) Tunable oxygen activation induced by oxygen defects in nitrogen doped carbon quantum dots for sustainable boosting photocatalysis. Carbon 114:601–607. https://doi.org/10.1016/j.carbon.2016.12.030